Detection of atmospheric species and dynamics in the bloated hot Jupiter WASP-172 b with ESPRESSO

A&A, 678, A150 (2023)
https://doi.org/10.1051/0004-6361/202347160

Astronomy & Astrophysics

Detection of atmospheric species and dynamics in the bloated hot Jupiter WASP-172 b with ESPRESSO⋆

J. V. Seidel[1,⋆⋆], B. Prinoth[1,2,⋆⋆⋆], E. Knudstrup[3,4], H. J. Hoeijmakers[2], J. J. Zanazzi[5,⋆⋆⋆⋆], and S. Albrecht[3]

[1] European Southern Observatory, Alonso de Córdova 3107, Vitacura, Región Metropolitana, Chile
e-mail: jseidel@eso.org
[2] Lund Observatory, Division of Astrophysics, Department of Physics, Lund University, Box 43, 221 00 Lund, Sweden
[3] Stellar Astrophysics Centre, Department of Physics and Astronomy, Aarhus University, Ny Munkegade 120, 8000 Aarhus C, Denmark
[4] Chalmers University of Technology, Department of Space, Earth and Environment, Chalmersplatsen 4, 412 93 Gothenburg, Sweden
[5] Astronomy Department and Center for Integrative Planetary Science, University of California Berkeley, 501 Campbell Hall, Berkeley, CA 94720, USA

Received 12 June 2023 / Accepted 25 August 2023

ABSTRACT

Context. The population of strongly irradiated Jupiter-sized planets has no equivalent in the Solar System. It is characterised by strongly bloated atmospheres and large atmospheric scale heights. Recent space-based observations of SO_2 photochemistry have demonstrated the knowledge that can be gained about Earth's uniqueness from detailed atmospheric studies of these unusual planets.
Aims. Here we explore the atmosphere of WASP-172 b, a planet similar in terms of temperature and bloating to the recently studied HD 149026 b. We characterise the atmospheric composition and subsequently the atmospheric dynamics of this prime target.
Methods. We observed a particular transit of WASP-172 b in front of its host star with ESO's ESPRESSO spectrograph and analysed the spectra obtained before, during, and after transit.
Results. We detect the absorption of starlight by WASP-172 b's atmosphere by sodium (5.6σ) and hydrogen (19.5σ) and obtained a tentative detection of iron (4.1σ). We detect strong – yet varying – blueshifts, relative to the planetary rest frame, of all of these absorption features. This allows for a preliminary study of the atmospheric dynamics of WASP-172 b.
Conclusions. With only one transit, we were able to detect a wide variety of species that clearly track different atmospheric layers with possible jets. WASP-172 b is a prime follow-up target for a more in-depth characterisation with both ground- and space-based observatories. If the detection of Fe is confirmed, this may suggest that radius inflation is an important determinant for the detectability of Fe in hot Jupiters, as several non-detections of Fe have been published for planets that are hotter but less inflated than WASP-172 b.

Key words. planets and satellites: atmospheres – planets and satellites: individual: WASP-172b – techniques: spectroscopic – methods: data analysis – line: profiles

1. Introduction

In comparison to the rest of the exoplanet population, hot Jupiters remain rare and are only found around approximately 1% of solar-type stars. Nonetheless, due to their intrinsically small semi-major axis, they are found ubiquitously via the transit method, including by the WASP[1] survey (Pollacco et al. 2006). They are characterised by strong irradiation from their host star and have no equivalent in the Solar System. Of the known hot Jupiters, fewer than two dozen have unequivocally confirmed atmospheres. Bloated hot Jupiters, with their large scale heights, make outstanding targets to further our knowledge of these strange objects.

WASP-172 b, one of the most bloated hot Jupiters found to date, is shown in the mass-insolation space in Fig. 1 (Hellier et al. 2019). WASP-172 b's host star is an F1V-type star (Vmag = 11.0, distance ~530 pc), which it orbits in 5.48 days (Hellier et al. 2019). It is one of the more bloated planets studied to date, with a mass of 0.47 M_J and a radius of 1.57 R_J, resulting in a mean density of only 0.16 ± 0.05 g cm^{-3} (see Table 1 for an overview of the system parameters).

In this work we provide the first evidence of various atmospheric detections from one ESPRESSO[2] transit for WASP-172 b, demonstrating its potential as a target for additional in-depth study. This paper is structured as follows: in Sect. 2 we provide an overview of the ESPRESSO dataset and discuss various possible contamination sources and corrections, followed by the detections obtained with narrow-band transmission spectroscopy (Sect. 3) and cross-correlation analysis (Sect. 4). We then discuss our findings and provide an outlook for future work in Sect. 5.

2. ESPRESSO dataset and initial analysis

We observed the bloated hot Jupiter WASP-172 b with the ESPRESSO echelle spectrograph at ESO's VLT[3] in Paranal

⋆ Based on observations made at ESO's VLT (ESO Paranal Observatory, Chile) accessible under ESO programme 109.22Z4.006 (PI: Albrecht).
⋆⋆ ESO Fellow, joint first author.
⋆⋆⋆ Joint first author.
⋆⋆⋆⋆ 51 Pegasi b Fellow.
[1] Wide Angle Search for Planets.
[2] Echelle SPectrograph for Rocky Exoplanets and Stable Spectroscopic Observations.
[3] Very Large Telescope.

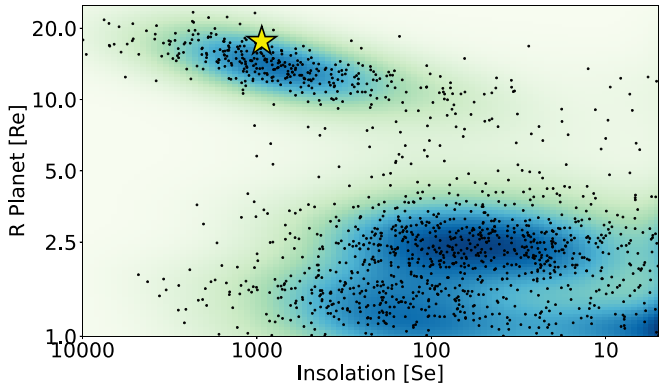

Fig. 1. Bloated hot Jupiter WASP-172 b shown as a yellow star in the mass vs. insolation space in Earth units. The data were retrieved from the NASA Exoplanet Archive at https://exoplanetarchive.ipac.caltech.edu/.

Observatory, Chile (Pepe et al. 2021) on the night of 2022 June 01 as part of ESO programme 109.22Z4.006, PI: Albrecht. Figure 2 shows an overview of the observed transit.

In total, 31 spectra were observed, of which 20 were observed in transit. The first spectrum was taken with a shorter exposure time of 555 s instead of 900 s for testing purposes and weighed by their signal-to-noise ratio accordingly. Additionally, the target was observed until the end of its visibility at Paranal with airmass 2.6; however, the ESPRESSO Atmospheric Dispersion Corrector (ADC) is only calibrated for airmass <2.2. Therefore, the last three spectra (which had an airmass above 2.2) were rejected from the analysis, leaving a total of eight out-of-transit spectra for the narrow-band analysis, seven before transit and one after transit. For the cross-correlation analysis, we additionally removed the shorter exposure due to a visibly higher noise level. Cosmic rays were rejected at the 5σ level and replaced with the time-averaged mean (for more information, see e.g. Wyttenbach et al. 2015; Seidel et al. 2019).

Various effects had to be corrected before the planetary atmospheric signal can be extracted. We first corrected for telluric lines, which are mainly caused by O_2 around the sodium doublet and H_2O overall. We then studied the impact of telluric sodium emission and corrected for stellar effects.

We corrected the imprint of telluric absorption on our spectra with ESO's `molecfit`, version 1.5.1. (Smette et al. 2015; Kausch et al. 2015) with parameters as described in Allart et al. (2017). `molecfit` uses measured atmospheric conditions on-site during the observations and corrects micro-telluric and stronger telluric lines. Each individual spectrum is fit independently accounting for changing seeing and airmass during the time series. The thus-created telluric line profile is then divided from each spectrum. We checked the correction by visually assessing whether the before and after master spectra show any over or under-correction of known telluric lines around the sodium doublet where various strong telluric lines are present. For the cross-correlation technique, where wide wavelength ranges are needed rather than specific lines, the wavelength regions where the correction left visible residuals were masked out manually.

2.1. Telluric sodium emission

For the search for sodium, assessing the contribution of the sky emission is particularly important. We monitored for telluric sodium emission or sodium laser contamination with fibre B set on sky. No strong laser contamination in the sodium D_2 was found. However, in both the positions of the telluric sodium D_2 and D_1 line a sodium emission peak three times the noise level was found in the fibre B spectra, most notably at the end of the observations at higher airmass. The small magnitude of the emission lines together with the airmass dependence points towards the origin of meteor excitation of atmospheric sodium (Chen et al. 2020; Seidel et al. 2020b). Our observations coincided with the end of the 2022 τ-Herculids meteor shower, which was visible from Paranal at roughly 20 ° altitude just above the horizon[4]. These most affected spectra at the highest airmass were rejected from the analysis based on the ESPRESSO ADC restrictions and do not influence our results. For the remaining contamination,

Table 1. Summary of the stellar and planetary parameters of the WASP-172 system adopted in this study.

WASP-172 System parameters		
RA_{2000}	13:17:44	[2]
Dec_{2000}	−47:14:15	[2]
Parallax p [mas]	1.8942 ± 0.0222	[2]
Magnitude [V_{mag}]	11.0	[2]
Systemic velocity (v_{sys}) [km s^{-1}]	-20.283 ± 0.006	[1]
Stellar parameters		
Star radius (R_*) [$R_\odot$]	1.91 ± 0.10	[1]
Star mass (M_*) [$M_\odot$]	1.49 ± 0.07	[1]
Proj. rot. velocity ($v \sin i$) [km s^{-1}]	13.7 ± 1.0	[1]
Age [Gyr]	$1.2^{0.0}_{-1.2}$	[1]
Metallicity [Fe/H]	-0.10 ± 0.08	[1]
Planetary parameters		
Planet radius (R_p) [R_{Jup}]	1.57 ± 0.10	[1]
Planet mass (M_p) [M_{Jup}]	0.47 ± 0.10	[1]
Eq. temperature (T_{eq}) [K]	1740 ± 60	[1]
Density (ρ) [g cm^{-3}]	0.16 ± 0.05	[1]
Surface gravity ($\log g_p$) [cgs]	0.12 ± 0.04	[1]
Orbital and transit parameters		
Transit centre time (T_0) [HJD (UTC)]	2457032.2617 ± 0.0005	[1]
Orbital semi-major axis (a) [au]	0.06940 ± 0.00001	[1]
Scaled semi-major axis (a/R_*)	8.0 ± 0.5	[1]
Orbital inclination (i) [°]	86.7 ± 1.1	[1]
Projected orbital obliquity (λ) [°]	121 ± 13	[3]
Eclipse duration (T_{14}) [h]	5.294 ± 0.048	[1]
Radius ratio (R_p^2/R_*^2)	0.0072 ± 0.0002	[1]
RV semi-amplitude (K) [km s^{-1}]	0.042 ± 0.009	[1]
Period (P) [d]	5.477433 ± 0.000007	[1]
Eccentricity	$0^{+0.28}_{-0.00}$	[1]
Derived parameters		
Planetary orbital velocity (v_{orb}) [km s^{-1}]	137.8 ± 2.2	
Approx. scale height (H) [km]	1631 ± 56	
Transit depth of H ($\delta F/F$) [$\times 10^{-5}$]	20.9 ± 2.7	

References: [1] Hellier et al. (2019), [2] Gaia Collaboration (2020), [3] Knudstrup et al. (in prep.).

[4] https://spacetourismguide.com/tau-herculids-meteor-shower/

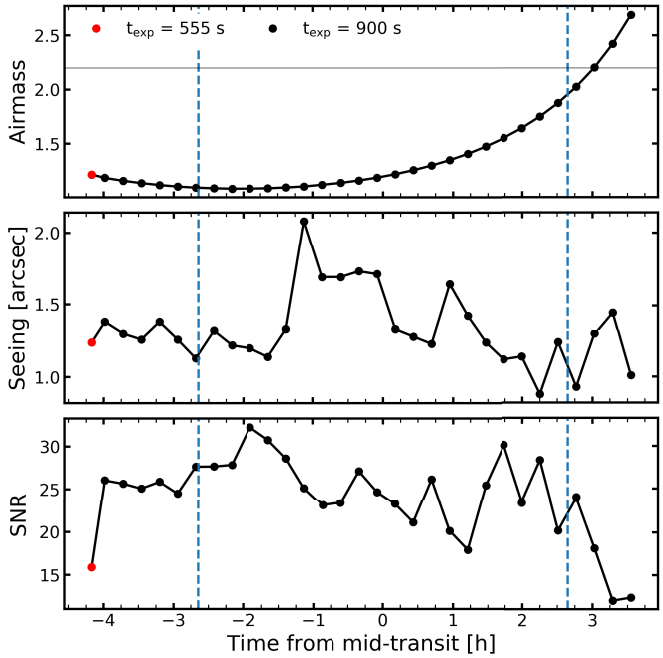

Fig. 2. Log of observations. Airmass (upper), seeing (middle), and signal-to-noise ratio in order 56 (bottom) during the time series. The vertical dashed blue lines indicate the start and the end of the transit. The first exposure has a shorter exposure time of 555 s. The grey horizontal line indicates the 2.2 airmass calibration limit of the ADC, based on which the three last exposures were rejected.

the line centres of the sodium emission do not overlap with the planetary trace. When taking into account the barycentric Earth radial velocity of approximately $-13\,\mathrm{km\,s^{-1}}$ during the entire transit, the centre of the remaining constant contamination in the stellar rest frame lies at 5889.25 and 5895.35 Å, respectively. For our overall transmission spectrum, the in-transit spectra are shifted in the planetary rest frame sequentially from $-28\,\mathrm{km\,s^{-1}}$ to $22\,\mathrm{km\,s^{-1}}$. This smears out the sodium emission contamination over a passband of roughly 1 Å around the stellar rest frame centres with no overlap with the planetary signal.

2.2. Stellar contamination

As the planet passes in front of the star it obscures part of the rotating stellar disc, leading to a distortion of the stellar spectral lines known as the Rossiter-McLaughlin (RM) and centre-to-limb variation (CLV) effects (Rossiter 1924; McLaughlin 1924; Triaud 2018; Albrecht et al. 2022). To properly account for this, we need to know the projected obliquity, λ, that is, the (projected) angle between the stellar spin axis and the orbital axis of the planet, in order to trace out the path of the planet in the local velocity field of the stellar surface. We did this by modelling the planetary shadow following the method by Albrecht et al. (2007), specifically as outlined in Knudstrup & Albrecht (2022). From this we obtained a value of $\lambda = 121 \pm 13$ deg (Knudstrup et al., in prep.). For narrow-band transmission spectroscopy, we then applied a numerical correction of the RM and CLV effects following Wyttenbach et al. (2020) with the local velocity field of the stellar surface to obtain the resolved planetary spectral features. For our cross-correlation analysis, as we need a correction for a much wider wavelength range, we model the radial velocity extent of the velocity component that is obscured by the planet during transit. This component is often termed Doppler shadow

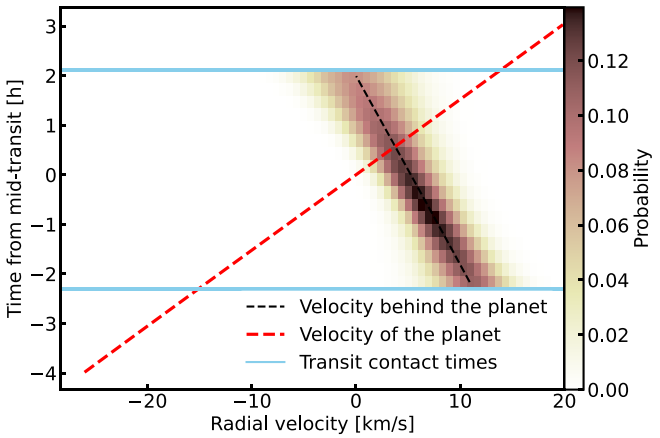

Fig. 3. Radial velocity extent of the velocity component obscured by the planet during transit. The dashed red line shows the expected planetary velocity. The blue lines indicate the start and the end of the transit. The dashed black line shows the mean radial velocity extent of the velocity component obscured by the planet during transit as predicted using 100 000 samples, assuming normal distributions for the planetary and stellar parameters (listed in Table 1).

and marked with a black dashed line in Fig. 3. Since the feature is not as prominent in cross-correlation space as for other systems (e.g. Hoeijmakers et al. 2020; Prinoth et al. 2022), we calculate the radial velocity extent expected for the feature following Cegla et al. (2016, see Eqs. (2)–(8) therein). Assuming normal distributions for the scaled semi-major axis a/R_s, the orbital inclination i, the projected orbital obliquity λ, the projected rotational velocity $v \sin i$ and no differential rotation, we drew 100 000 samples to calculate the possible traces of the residual of the obscuration (see Fig. 3). It is evident that the trace of the residual of the planetary obscuration of the stellar disc overlaps with the planetary trace for a short period of time after mid-transit. Using the expected radial velocity extent as our fitting prior, we model the feature as described in Sect. 4.

We did not perform any checks for rotational modulations, given that no significant rotational modulations of the host star were detected that could mimic an atmospheric signal (Hellier et al. 2019).

3. Narrow-band transmission spectroscopy

We calculate the transmission spectrum from the ESPRESSO transit following Tabernero et al. (2021); Borsa et al. (2021); Seidel et al. (2022), which we summarise here briefly. All spectra were weighted by their S/N and corrected for telluric lines. Then all spectra are shifted from the observer's rest frame to the stellar rest frame. In the stellar rest frame, the stellar spectral lines coincide at the same wavelengths and are removed from the magnitude-smaller planetary signal by dividing the in-transit spectra by the normalised sum of all out-of-transit spectra, the so-called master-out. The separated planetary spectra are then shifted into the planetary rest frame and combined for the final transmission spectrum. The velocities applied for the various reference frame changes are the barycentric earth radial velocity approximately $-13\,\mathrm{km\,s^{-1}}$, the planet velocity ranging from -28 to $22\,\mathrm{km\,s^{-1}}$, and a negligible stellar velocity of a few $\mathrm{m\,s^{-1}}$. The system velocity is $-20.28\,\mathrm{km\,s^{-1}}$ (taken from Hellier et al. 2019). The Coudé Train optics of ESPRESSO generate interference patterns, which create sinusoidal noise in the transmission spectra at the same order of magnitude as planetary lines (Allart et al. 2020; Tabernero et al. 2021). The true origin and dependence on

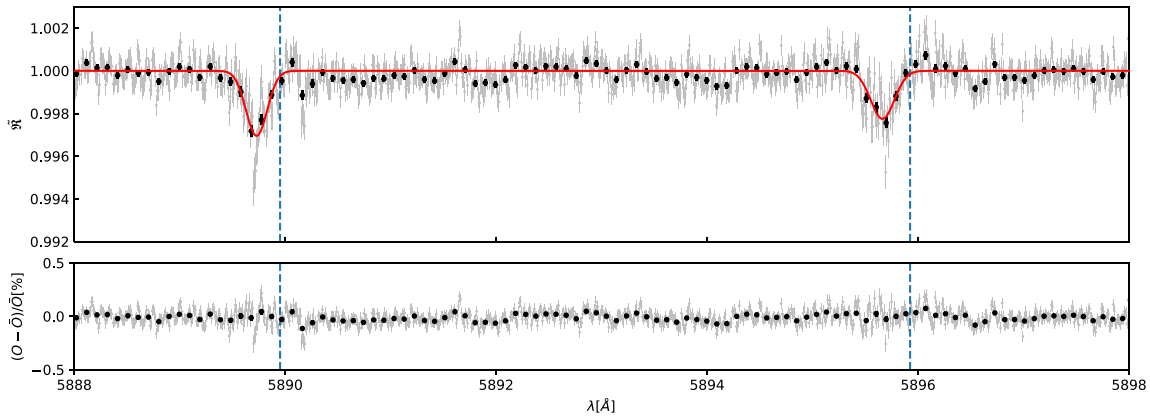

Fig. 4. ESPRESSO transmission spectrum of WASP-172 b for the sodium doublet in the planetary rest frame. Upper panel: transmission spectrum in full resolution (in grey) and the same data binned by ×20 (in black). The data have been corrected for tellurics, cosmics, and the RM+CLV effect. The rest frame transition wavelengths are marked with dashed blue lines. A Gaussian fit to both lines simultaneously is shown in red. Lower panel: residuals of the Gaussian fit.

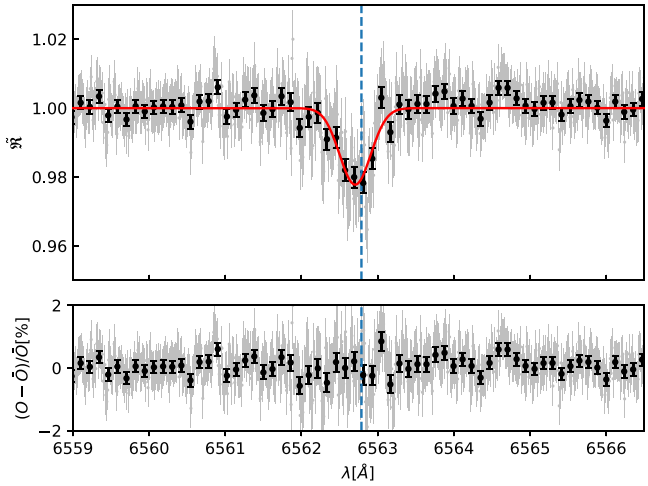

Fig. 5. ESPRESSO transmission spectrum of WASP-172 b for the wavelength range of the H-α line in the planetary rest frame. Upper panel: transmission spectrum in full resolution (in grey) and the same data binned by ×20 (in black). The data have been corrected for tellurics, cosmics, and the RM+CLV effect. The rest frame transition wavelength is marked with a dashed blue line. A Gaussian fit is shown in red. Lower panel: residuals of the Gaussian fit.

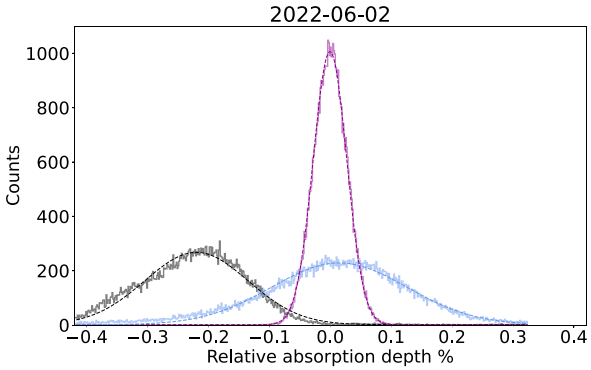

Fig. 6. Distribution of the bootstrapping analysis for the 12 Å passband around the sodium doublet for 50 000 random selections. The in-in (magenta) and out-out (light blue) distributions are centred at zero (no planetary sodium detection), and the in-out distribution, indicating a planetary origin of the feature, is shown in black.

airmass and other factors are not yet fully understood, but efforts are currently underway to correct this behaviour on the pipeline level (priv. comm.). In the orders of the sodium doublet and the H-α line, no notable wiggles were visible; however, it is likely that the much stronger low-frequency wiggles in other orders inhibited the detection of other resolved spectral lines (e.g. in the order of Li). Once the pipeline is able to mitigate this interference pattern, the analysis presented here should be expanded to include species that we could not detect.

We show the transmission spectra of sodium and H-α in Figs. 4 and 5, combining the two spectral orders that independently contain the wavelength range of interest: 116 and 117 for the sodium doublet and 138 and 139 for H-α. The Gaussian fit shown for both figures (in red) is generated on the unbinned data (in grey) with width, depth, and position as free parameters.

3.1. False positive assessment

A false positive detection can arise from instrumental effects, stellar spots, or the variation of observational conditions during the night. The false positive probability can be calculated via a bootstrap analysis with an empirical Monte Carlo (Redfield et al. 2008). The false positive probability is then directly taken into account when calculating the detection error.

To understand whether only the assessment presented here of in- and out-of-transit data yields a detection, in- and out-of-transit data were considered as two independent datasets; only the in-transit data should contain real traces of the planetary signature. Following the approach in Redfield et al. (2008), virtual transmission spectra are created by randomly drawing new virtual in-transit and out-of-transit datasets from our real data. We distinguish between three scenarios: 'in-in' (all spectra taken from the real in-transit data and randomly attributed to virtual in and out-of-transit data), 'out-out' (drawn only from out-of-transit spectra), and 'in-out', where virtual in-transit is drawn from real in-transit and vice versa for the out-of-transit pair. If the detection truly stems from the planetary atmosphere and is not a spurious event, only the in-out scenario should yield a significant result.

From this assessment, we calculate the false positive likelihood as the standard deviation of the out-out distribution. The out-out distribution is used as it does not contain any actual planetary signal and a detection in this dataset would be a true false positive. To mitigate the inherent selection bias of this method, the likelihood has to be scaled by the square root of the fraction

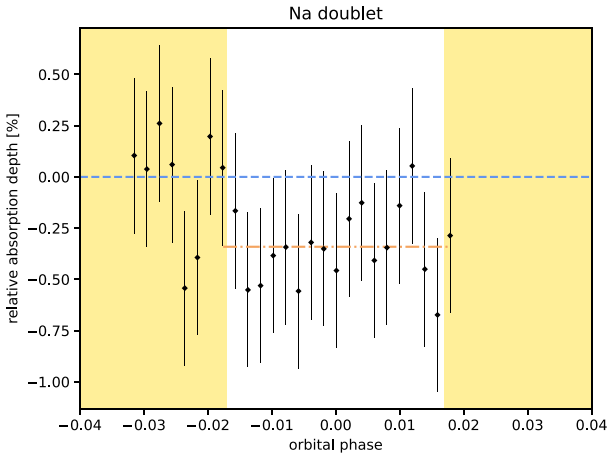

Fig. 7. Relative absorption of the sodium doublet in the planetary rest frame as a function of phase. The dashed blue line shows the neutral 0.0, the dashed-dotted brown line shows the in-transit mean, and the shaded areas mark the out-of-transit phases.

Table 2. Narrow-band detection levels.

	Detection [%]	σ
Na D_2	0.305 ± 0.067	4.5
Na D_1	0.225 ± 0.068	3.3
Combined	0.265 ± 0.048	5.6
H-α	2.222 ± 0.114	19.5

of out-of-transit spectra to total spectra taken (Redfield et al. 2008; Astudillo-Defru & Rojo 2013).

The bootstrapping distribution for the sodium doublet is shown in Fig. 6, with 50 000 iterations. The in-in and out-out distributions are centred at 0, ruling out spurious features as the cause for our detections. The in-out distribution is centred at −0.22%, highlighting that the signal origins only from the in-transit exposures and shows uniformity. This analysis also shows that the sodium detection is not influenced by the sodium emission contamination described in Sect. 2. The false positive likelihood for the analysed transit is 8.5×10^{-4}.

To additionally assess whether the sodium detection stems truly from the planet and not from stellar phenomena we created the relative absorption light curve for sodium (see Fig. 7) showing the extra drop in flux for the in-transit spectra when integrating over the wavelength range of the sodium doublet, following Seidel et al. (2019). We can clearly see a marked extra drop in flux during transit (highlighted by the brown, dashed-dotted mean), but it also highlights the limitations of the dataset with a short out-of-transit baseline only before the transit.

3.2. Atmospheric detection levels

We searched for resolved spectral lines of Na, H-α, Mg, Li, and K and were able to unambiguously detect the sodium doublet (shown in Fig. 4; 5.6σ detection for both lines combined) and the H-α line of the Balmer-series of hydrogen (shown in Fig. 5; 19.5σ detection). Both spectral ranges are shown in the planetary rest frame and the expected line centres are indicated as dashed blue vertical lines. Gaussian fits to the spectral ranges are shown in red. The amplitude of the fit was used to estimate the absorption depth in Table 2 while the uncertainty is composed of the uncertainty of the Gaussian fit, the average uncertainty within the full width at half maximum (FWHM) of the detected lines, and the false positive likelihood calculated in Sect. 3.1 following Hoeijmakers et al. (2020).

While the two detections are unambiguous, a study of the line shape relies on confirmation of the results presented here. There is currently no second transit of this target available as the here presented dataset is part of an exploratory programme geared towards understanding system architectures via the RM effect with only one transit per target. However, the H-α and sodium lines both show curiously different blueshifted offsets, which are discussed in Sect. 5.2 without an in-depth analysis of atmospheric dynamics.

4. Cross-correlation analysis

We further analysed the transit time series using the cross-correlation technique (Snellen et al. 2010) following the methodology in Prinoth et al. (2022). After telluric correction as described in Sect. 2, the individual spectra are shifted to the rest frame of the host star. The Doppler shifts include corrections for the Earth's velocity around the barycentre of the Solar System and the radial velocity of the host star caused by the orbiting planet. The velocity corrections yield a stellar spectrum with a constant velocity shift that is consistent with the systemic velocity of $-20.283 \pm 0.006\,\mathrm{km\,s^{-1}}$. To account for outliers, we follow Hoeijmakers et al. (2020) and apply an order-by-order sigma clipping algorithm that computes a running median absolute deviation over sub-bands of the time series spanning 40 pixels in width. Pixels with deviations larger than 5σ-outliers were rejected and interpolated. Additionally, we flagged spectral columns where the telluric correction left systematic noise, mainly caused by deep telluric lines. The rejection of outliers and manual masking of spectral pixels affected 7.81% of the pixels in the time series. Using cross-correlation templates at 2000 and 4000 K from Kitzmann et al. (2023), we searched for H, Fe, Na, Mg, Ca, Li, K, Ti, and V. Although the planet's equilibrium temperature is below 2000 K, we eventually settled for the 4000 K templates to avoid pressure broadening, which is relatively strong in the cooler templates of our species due to higher abundance.

For model comparison, we injected a model of the expected transmission spectrum for WASP-172 b at the 2000 and 3000 K ($T_{\rm eq}$ =1740 K; Hellier et al. 2019). The model assumes the planetary atmosphere to be isothermal, in chemical and hydrostatical equilibrium, and at solar metallicity. The planetary parameters are listed in Table 1. We computed the chemical abundance profiles with `FastChem` (Stock et al. 2018), which accounts for the variations of molecular weight with altitude, and used these to model the transmission spectrum with `petitRADTRANS` (Mollière et al. 2015), where we included line absorption from Ca, Cr, Fe, Fe^+, K, Na, Ti, and V. The line lists for the species in the model were taken from Piskunov et al. (1995) and Ryabchikova et al. (2015)[5], H_2-H_2 and H_2-He were considered for the collision-induced absorption, and H_2 and He were loaded for Rayleigh scattering.

To fit for the residual of the planetary obscuration of the stellar disc during transit, we constructed an empirical model of Fe by fitting a double Gaussian, similar to Prinoth et al. (2022). The correction steps for the planetary obscuration of the stellar disc are shown in Fig. A.1. Finally, we applied a high-pass filter to correct for any residual broadband variations before converting

[5] See https://petitradtrans.readthedocs.io/en/latest/content/available_opacities.html

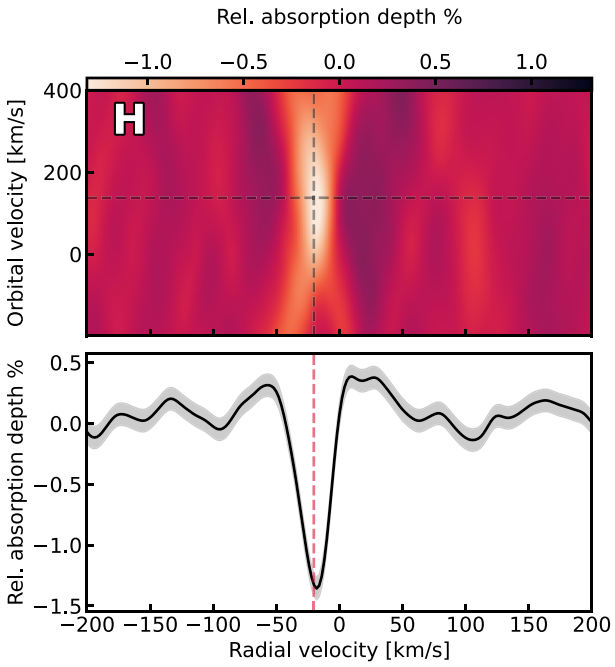

Fig. 8. Cross-correlation result for H in the atmosphere of WASP-172 b. Top panel: $K_p - V_{sys}$ diagram for H. The dashed grey lines indicate the true orbital and systemic velocities of 137.8 ± 2.2 km s^{-1} and -20.283 ± 0.006 km s^{-1}, respectively. The absorption feature appears at the expected location. Bottom panel: one-dimensional cross-correlation function at the true orbital velocity. The vertical dashed pink line indicates the true systemic velocity, the same as in the upper panel.

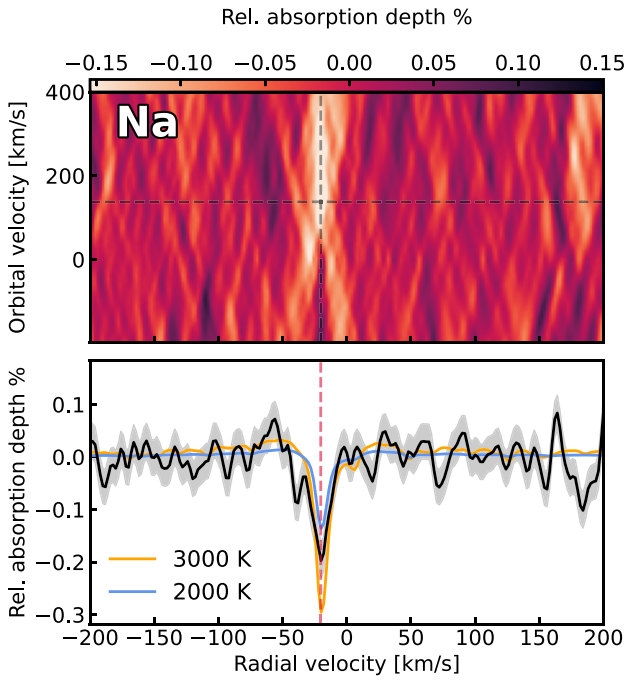

Fig. 9. Same as Fig. 8 but for Na. The blue and orange lines show the predicted relative absorption depth for the models at 2000 and 3000 K, respectively.

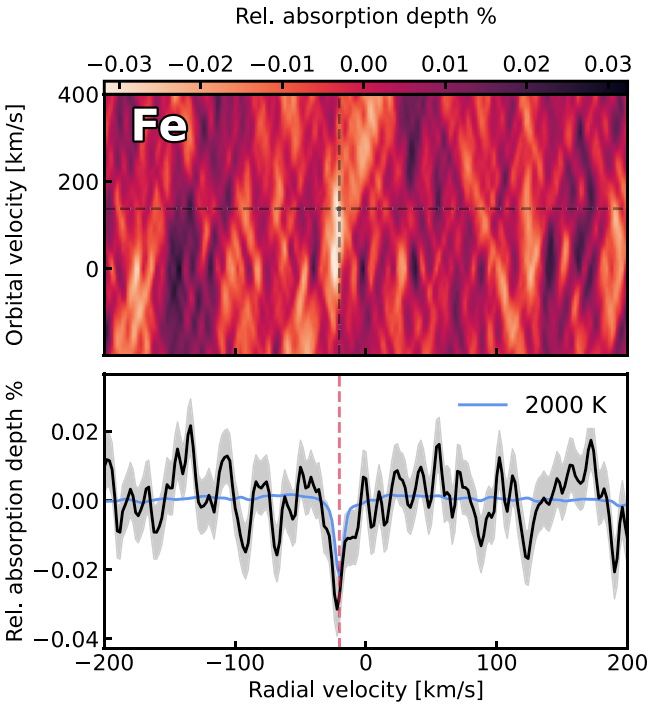

Fig. 10. Same as Fig. 8 but for Fe. The blue shows the predicted relative absorption depth for the model at 2000 K. The model prediction for 3000 K is not shown due to the large predicted absorption depth (~0.5%).

the cross-correlation maps into $K_p - V_{sys}$ maps (see Hoeijmakers et al. 2020 and Prinoth et al. 2022 for an extensive discussion).

Using the cross-correlation technique, we detect H, Na, and Fe in the transmission spectrum of WASP-172 b. The detections are shown in Figs. 8–10 in $K_p - V_{sys}$ space. While the detection of H aligns with the expected orbital and systemic velocity, the detection of Fe shows residuals from removing the signal of the planetary obscuration of the stellar disc during transit. Due to the relatively low orbital velocity of the planet of only 137.0 ± 2.2 km s^{-1}, caution should be taken when interpreting this detection as contamination from the residual of the planetary obscuration during transit which may increase the observed signal. However, because the velocity traces of the planet and the obscured stellar disc are in opposing directions, contamination of any signal originating from the planet's atmosphere is minimised. This architecture makes WASP-172 b a favourable system for high-resolution transmission spectroscopy.

To test whether the signal originates uniformly from in-transit exposures and that it does not appear in out-of-transit exposures, we performed a similar false-positive assessment as described in Sect. 3.1. Instead of wavelength space, we used radial velocity space, which allowed us to perform the false-positive analysis directly on the two-dimensional cross-correlation function. The variation for cross-correlation space is described in detail in Appendix A of Hoeijmakers et al. (2020). Figures 11–13 show the result of the false-positive assessment for the detected species.

5. Discussion and conclusions

5.1. Atmospheric composition

Fe is known to be a strong absorber in the atmospheres of (ultra-)hot Jupiters and is nowadays routinely detected using the cross-correlation technique (e.g. Hoeijmakers et al. 2018, 2020; Stangret et al. 2020; Prinoth et al. 2022; Kesseli et al. 2022). The injected model at a temperature of 2000 K matches the observed absorption depth for Fe, while Na requires a model at a higher temperature. The injected models all have a higher temperature than the equilibrium temperature of this planet (1740 ± 60 K), suggesting that the temperature at the terminator exceeds the

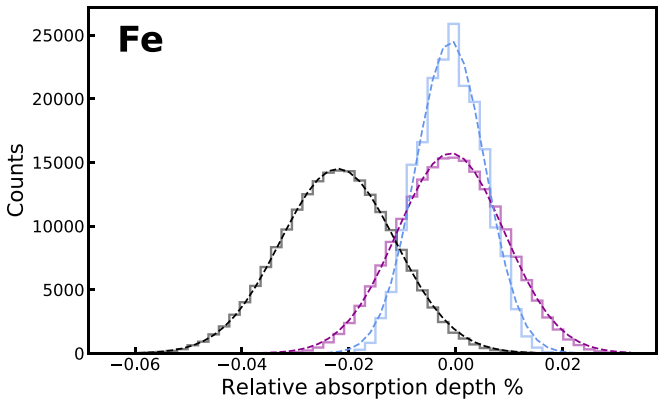

Fig. 11. Distribution of bootstrapping analysis for 200,000 random selections. Similar to Fig. 6, the in-in (magenta) and out-out (light-blue) distributions are centred around zero, indicating the absence of Fe. The in-out distribution in black shows the planetary origin of the feature. For the out-out distribution, we only include the seven out-of-transit exposures that were considered in the cross-correlation analysis.

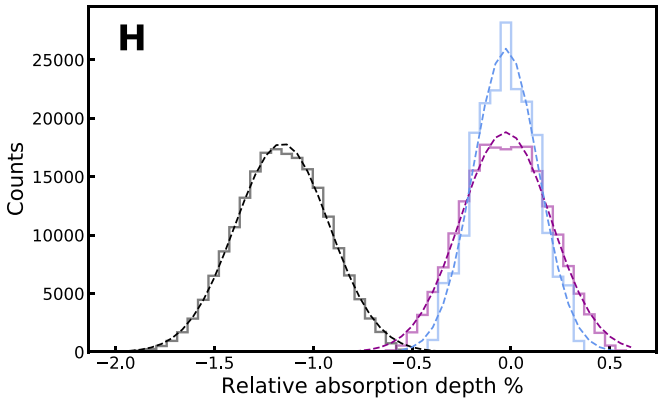

Fig. 12. Same as Fig. 11 but for H.

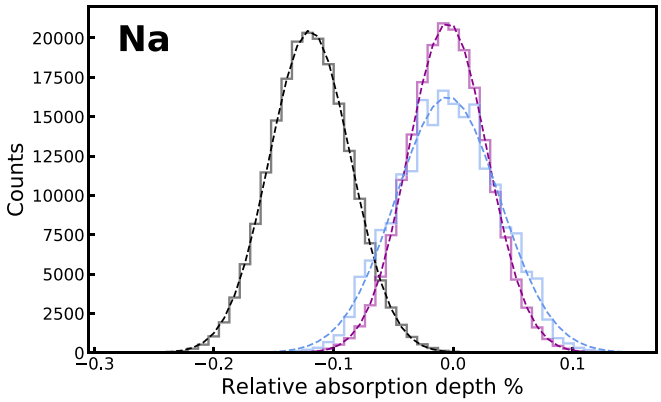

Fig. 13. Same as Fig. 11 but for Na.

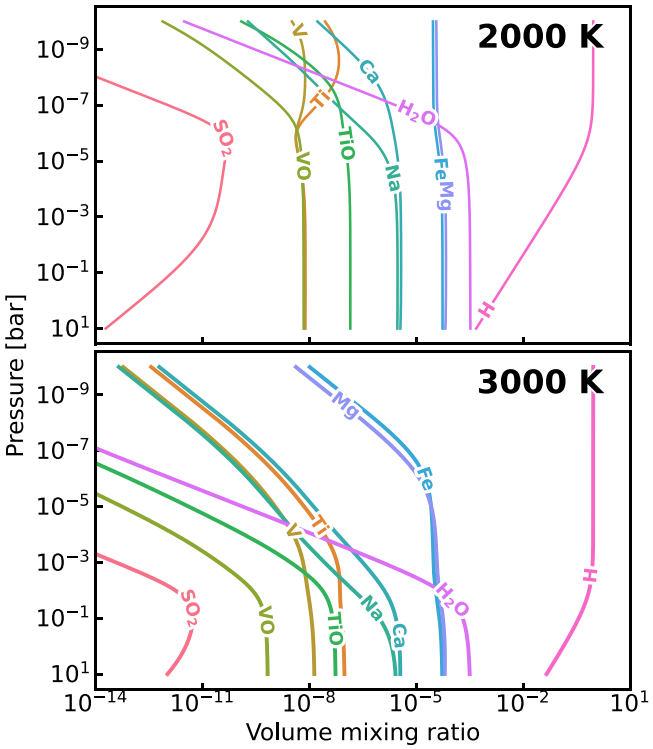

Fig. 14. Model of the abundances of key selected species as a function of pressure (inverse altitude) at a temperature of 2000 (top) and 3000 K (bottom), assuming thermo-chemical equilibrium and solar metallicity. The abundance profiles were computed with `FastChem` (Stock et al. 2018).

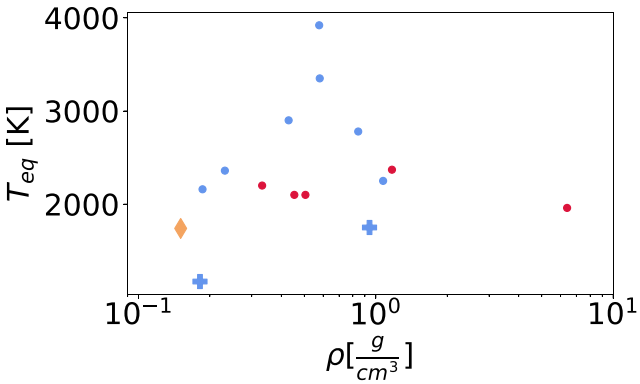

Fig. 15. WASP-172 b in temperature-density space together with all currently known Fe detections in blue for exoplanets with confirmed Fe, as well as known upper limits in red. We have limited the data to exoplanets with a well-constrained mass. Already observed JWST targets in the lower temperature range are marked with crosses (HD 149026 b and WASP-39 b), and WASP-172 b is marked as a brown diamond. From `http://research.iac.es/proyecto/exoatmospheres/table.php`, retrieved in August 2023.

equilibrium temperature and/or that the atmosphere is more extended than expected from the hydrostatic equilibrium frequently observed in hotter, ultra-hot Jupiters (e.g. Hoeijmakers et al. 2019). Figure 14 shows the expected abundances of selected species as a function of pressure (inverse altitude) for both 2000 and 3000 K. Fe and Mg are expected to be abundant at relatively high altitudes, while other metals thermally ionise above approximately 1 µbar at 2000 K or 1 mbar at 3000 K. Like Na, the absorption spectrum of Mg is dominated by a few strong absorption lines, making the application of cross-correlation less effective than for elements with richer spectra. Fe absorbs over the whole wavelength range of ESPRESSO, but individual lines are intrinsically weaker than the resonant lines of the alkali metals. Even at 2000 K, molecular hydrogen significantly dissociates at pressures below 1 mbar, meaning that the atmosphere at the terminator transitions from molecular to atomic over the altitude range probed by the transmission spectrum. This explains why deep single lines of Na are detectable in the transmission spectrum while the much richer spectrum of Fe results in a

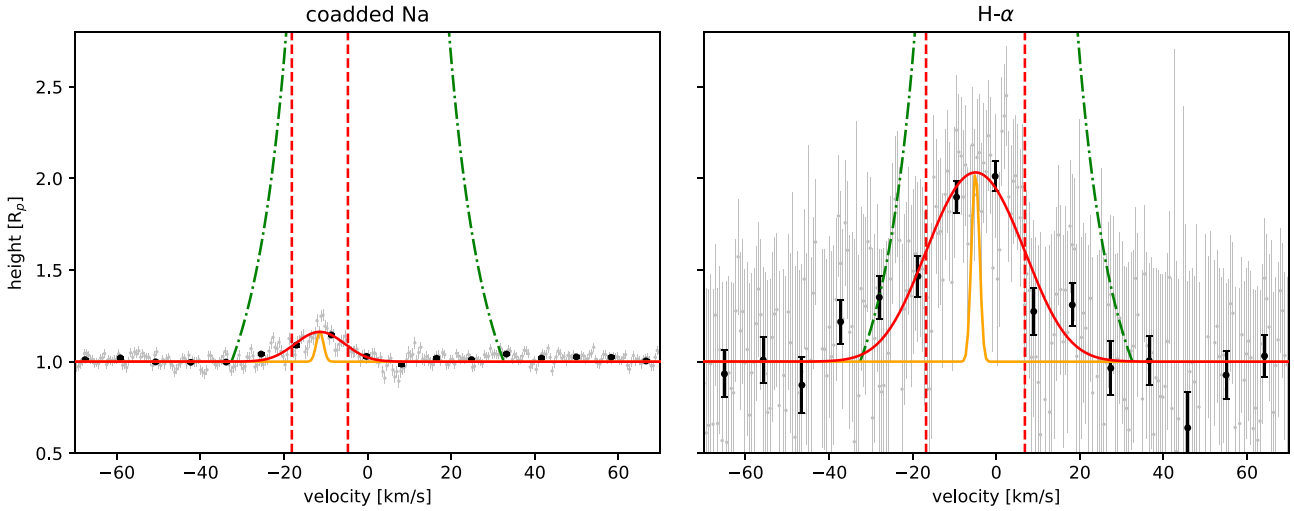

Fig. 16. Co-added sodium doublet and the H-α line in velocity space as a function of altitude above the white light radius. The Gaussian fits together with the FWHM (dashed vertical lines) is shown in red, the ESPRESSO line spread function in yellow, and the escape velocity as a function of height in dashed-dotted green.

relatively marginal detection. The lines of Fe are intrinsically weaker, meaning that they are formed at lower altitudes, where the atmospheric scale height is approximately a factor of two smaller.

Even though the signal of Fe is offset from the system rest-frame velocity (see the velocity-velocity diagram in Fig. 10), due to the relatively low planetary radial velocity (see Fig. 3), the signal of Fe may still be consistent with the rest-frame velocity of the star. This could in theory indicate a stellar origin. To better constrain the velocity, more transit observations would be required to confirm the detection of Fe in the transmission spectrum of WASP-172 b. If confirmed, the detection of Fe in the transmission spectrum of WASP-172 b adds to the detections for heavily inflated hot Jupiters (see Fig. 15). Importantly, because WASP-172 b is a relatively cold planet that is not regarded as an ultra-hot Jupiter (typical definitions place the boundary above 2000 K), a robust confirmation of Fe would have implications for our understanding of the chemistry of planets that straddle the hot-ultra–hot Jupiter boundary.

Recently, Stangret et al. (2022) reported the non-detection of Fe in the atmosphere of KELT-17 b with the HARPS spectrograph, a planet with a higher equilibrium temperature but a less inflated atmosphere. The host star KELT-17 b is a variable Am star and is subject to pulsations, so a detailed analysis is difficult (Saffe et al. 2020). Fe was similarly not detected in the atmosphere of the hotter but less inflated WASP-19 b (Sedaghati et al. 2021) after multiple transit observations with ESPRESSO. This suggests that planets that are less inflated require a higher equilibrium temperature for Fe absorption to be significantly detectable. The planet with the lowest temperature and reported Fe detection is HD 142096 b (Ishizuka et al. 2021), an inflated hot Jupiter that is similar to WASP-172 b, with a dayside temperature of ∼2100 K. However, this detection is only confirmed at the 2.8σ level. From both similar targets in the literature and this work, it is therefore unclear whether neutral iron is present in inflated, but cooler, hot Jupiters, and follow-up observations are crucial. Na and H are detected with high significance using both narrow-band transmission spectroscopy and the cross-correlation technique.

5.2. Atmospheric dynamics

In the two species detected via narrow-band transmission spectroscopy, a clear blueshift is detectable. The sodium doublet in air is expected at 5889.950 and 5895.924 Å, but the Gaussian fit in our data sets the centre of the lines at 5889.728 ± 0.011 and 5895.663 ± 0.016 Å, respectively. This corresponds to a blueshift towards the observer of 11.3 and 13.2 km s^{-1}, respectively. Both sodium lines should be shifted in the same way, and the difference in observed blueshift highlights the ambiguity of the line shape for atmospheric studies. A dedicated observation of this target geared towards atmospheric dynamics will remedy this shortcoming. Sodium traces the atmosphere from the lower atmosphere at the micro-bar pressure level up to the start of potential inversion layers in a thermosphere (Wyttenbach et al. 2015; Seidel et al. 2020a), while H-α as the main hydrogen line traces the atmosphere in its full vertical extension. H-α is expected in air at 6562.810 Å but is detected here at 6562.705 ± 0.01 Å. This shift corresponds to a movement towards the observer at 4.8 km s^{-1}. Assuming that WASP-172 b is tidally locked, the rotational velocity of the atmosphere is approximately 1.5 km s^{-1}. In broad terms, integrated over the entire atmosphere as traced by H-α and taking the planetary rotation into account, the atmosphere shows a movement from the hot dayside facing the star towards the cooler nightside of ∼3−6 km s^{-1}. The sodium doublet, which traces largely lower layers of the atmosphere in comparison, shows the same overall movement at higher wind speeds between ∼10 and 14 km s^{-1}. The difference in wind speeds at the different altitude levels hints at high-velocity day-to-nightside winds that might be localised in jet streams at the micro-bar level and above, as seen for a wide range of Jupiter-like planets, from emission features on the hottest planet ever found, KELT-9 b (Pino et al. 2022), to ultra-hot Jupiters (Ehrenreich et al. 2020; Kesseli & Snellen 2021; Seidel et al. 2021, 2023; Gandhi et al. 2022, 2023; Brogi et al. 2023), to the cooler end of hot Jupiters, for example HD 189733 b (Seidel et al. 2020a).

Compared to the line spread function of the instrument, both the sodium doublet and the H-α line are broadened significantly,

with a FWHM of 13.4 and 23.6 km s^{-1}, respectively (see Fig. 16). This broadening is indicative of either a super-rotational wind in the entire atmosphere or a radial, vertical wind pattern moving outwards. However, despite the low mass of the planet, neither species moves beyond the escape velocity, indicating a stable atmosphere. However, understanding atmospheric dynamics from Doppler shifts requires a high level of confidence not only in the detection but also in the line shape and position. As stated before for the two lines of the sodium doublet, the uncertainty on the shift is most likely of the order of several km s^{-1}, and without further data it is unclear if the observed resolved lines are truly at significantly different velocities. It is encouraging that similar shifts are seen with the cross-correlation technique, which implies that there was no artificial shift introduced in the narrow-band transmission spectra by the data reduction method. Nonetheless, follow-up observations with a more reliable out-of-transit baseline to prove the repeatability of the observations are crucial for a more in-depth study of the atmospheric dynamics of WASP-172 b.

5.3. Future avenues

Considering that we only have one transit available and cannot confidently resolve the line shape, it is not possible to properly understand which kind of wind pattern generates the offsets we see here; a day-to-nightside wind is as possible as a one-sided jet or a super-rotational wind stream. However, the clear offsets in multiple lines, as well as the clear detection in the cross-correlation function, make WASP-172 b a prime candidate for time-resolved transit observations that can be used to bridge the transition from hot to ultra-hot Jupiters. In Fig. 15, WASP-172 b is shown together with all currently known exoplanets with confirmed or tentative iron detections that also have well-constrained masses and, therefore, densities. The two other exoplanets in the same lower temperature range of hot Jupiters, HD 149026 b and WASP-39 b, are marked with crosses and have been, coincidentally, observed with JWST.

WASP-39 b has provided an outstanding target with a clear detection of H_2O (Alderson et al. 2023) as well as the first detection of photochemical processes in an exoplanet via SO_2 (Alderson et al. 2023; Tsai et al. 2023). HD 149026 b has similarly shown high metal enrichment (Bean et al. 2023), highlighting the potential of the similar WASP-172 b for follow-up with ground- and space-based facilities to broaden our understanding of the transition from ultra-hot to cooler hot Jupiters.

Acknowledgements. The authors acknowledge the ESPRESSO project team for its effort and dedication in building the ESPRESSO instrument. This work relied on observations collected at the European Organisation for Astronomical Research in the Southern Hemisphere. S.A. acknowledges the support from the Danish Council for Independent Research through a DFF Research Project 1 grant, No. 2032-00230B.

References

Albrecht, S., Reffert, S., Snellen, I., Quirrenbach, A., & Mitchell, D. S. 2007, A&A, 474, 565
Albrecht, S. H., Dawson, R. I., & Winn, J. N. 2022, PASP, 134, 082001
Alderson, L., Wakeford, H. R., Alam, M. K., et al. 2023, Nature, 614, 664
Allart, R., Lovis, C., Pino, L., et al. 2017, A&A, 606, A144
Allart, R., Pino, L., Lovis, C., et al. 2020, A&A, 644, A155
Astudillo-Defru, N., & Rojo, P. 2013, A&A, 557, A56
Bean, J. L., Xue, Q., August, P. C., et al. 2023, Nature, 618, 43
Borsa, F., Allart, R., Casasayas-Barris, N., et al. 2021, A&A, 645, A24
Brogi, M., Emeka-Okafor, V., Line, M. R., et al. 2023, AJ, 165, 91
Cegla, H. M., Lovis, C., Bourrier, V., et al. 2016, A&A, 588, A127
Chen, G., Casasayas-Barris, N., Pallé, E., et al. 2020, A&A, 635, A171
Ehrenreich, D., Lovis, C., Allart, R., et al. 2020, Nature, 580, 597
Gaia Collaboration 2020, VizieR Online Data Catalog: I/350
Gandhi, S., Kesseli, A., Snellen, I., et al. 2022, MNRAS, 515, 749
Gandhi, S., Kesseli, A., Zhang, Y., et al. 2023, AJ, 165, 242
Hellier, C., Anderson, D. R., Bouchy, F., et al. 2019, MNRAS, 482, 1379
Hoeijmakers, H. J., Ehrenreich, D., Heng, K., et al. 2018, Nature, 560, 453
Hoeijmakers, H. J., Ehrenreich, D., Kitzmann, D., et al. 2019, A&A, 627, A165
Hoeijmakers, H. J., Seidel, J. V., Pino, L., et al. 2020, A&A, 641, A123
Ishizuka, M., Kawahara, H., Nugroho, S. K., et al. 2021, AJ, 161, 153
Kausch, W., Noll, S., Smette, A., et al. 2015, A&A, 576, A78
Kesseli, A. Y., & Snellen, I. A. G. 2021, ApJ, 908, L17
Kesseli, A. Y., Snellen, I. A. G., Casasayas-Barris, N., Mollière, P., & Sánchez-López, A. 2022, AJ, 163, 107
Kitzmann, D., Hoeijmakers, H. J., Grimm, S. L., et al. 2023, A&A, 669, A113
Knudstrup, E., & Albrecht, S. H. 2022, A&A, 660, A99
McLaughlin, D. B. 1924, Popular Astron., 32, 225
Mollière, P., van Boekel, R., Dullemond, C., Henning, T., & Mordasini, C. 2015, ApJ, 813, 47
Pepe, F., Cristiani, S., Rebolo, R., et al. 2021, A&A, 645, A96
Pino, L., Brogi, M., Désert, J. M., et al. 2022, A&A, 668, A176
Piskunov, N. E., Kupka, F., Ryabchikova, T. A., Weiss, W. W., & Jeffery, C. S. 1995, A&AS, 112, 525
Pollacco, D. L., Skillen, I., Collier Cameron, A., et al. 2006, PASP, 118, 1407
Prinoth, B., Hoeijmakers, H. J., Kitzmann, D., et al. 2022, Nat. Astron., 6, 449
Redfield, S., Endl, M., Cochran, W. D., & Koesterke, L. 2008, ApJ, 673, L87
Rossiter, R. A. 1924, ApJ, 60, 15
Ryabchikova, T., Piskunov, N., Kurucz, R., et al. 2015, Phys. Scrip., 90, 054005
Saffe, C., Miquelarena, P., Alacoria, J., et al. 2020, A&A, 641, A145
Sedaghati, E., MacDonald, R. J., Casasayas-Barris, N., et al. 2021, MNRAS, 505, 435
Seidel, J. V., Ehrenreich, D., Wyttenbach, A., et al. 2019, A&A, 623, A166
Seidel, J. V., Ehrenreich, D., Pino, L., et al. 2020a, A&A, 633, A86
Seidel, J. V., Lendl, M., Bourrier, V., et al. 2020b, A&A, 643, A45
Seidel, J. V., Ehrenreich, D., Allart, R., et al. 2021, A&A, 653, A73
Seidel, J. V., Cegla, H. M., Doyle, L., et al. 2022, MNRAS, 513, L15
Seidel, J. V., Borsa, F., Pino, L., et al. 2023, A&A, 673, A125
Smette, A., Sana, H., Noll, S., et al. 2015, A&A, 576, A77
Snellen, I. A. G., de Kok, R. J., de Mooij, E. J. W., & Albrecht, S. 2010, Nature, 465, 1049
Stangret, M., Casasayas-Barris, N., Pallé, E., et al. 2020, A&A, 638, A26
Stangret, M., Casasayas-Barris, N., Pallé, E., et al. 2022, A&A, 662, A101
Stock, J. W., Kitzmann, D., Patzer, A. B. C., & Sedlmayr, E. 2018, MNRAS, 479, 865
Tabernero, H. M., Zapatero Osorio, M. R., Allart, R., et al. 2021, A&A, 646, A158
Triaud, A. H. M. J. 2018, in Handbook of Exoplanets, eds. H. J. Deeg, & J. A. Belmonte (Berlin: Springer), 2
Tsai, S.-M., Lee, E. K. H., Powell, D., et al. 2023, Nature, 617, 483
Wyttenbach, A., Ehrenreich, D., Lovis, C., Udry, S., & Pepe, F. 2015, A&A, 577, A62
Wyttenbach, A., Mollière, P., Ehrenreich, D., et al. 2020, A&A, 638, A87

Appendix A: Cross-correlation map

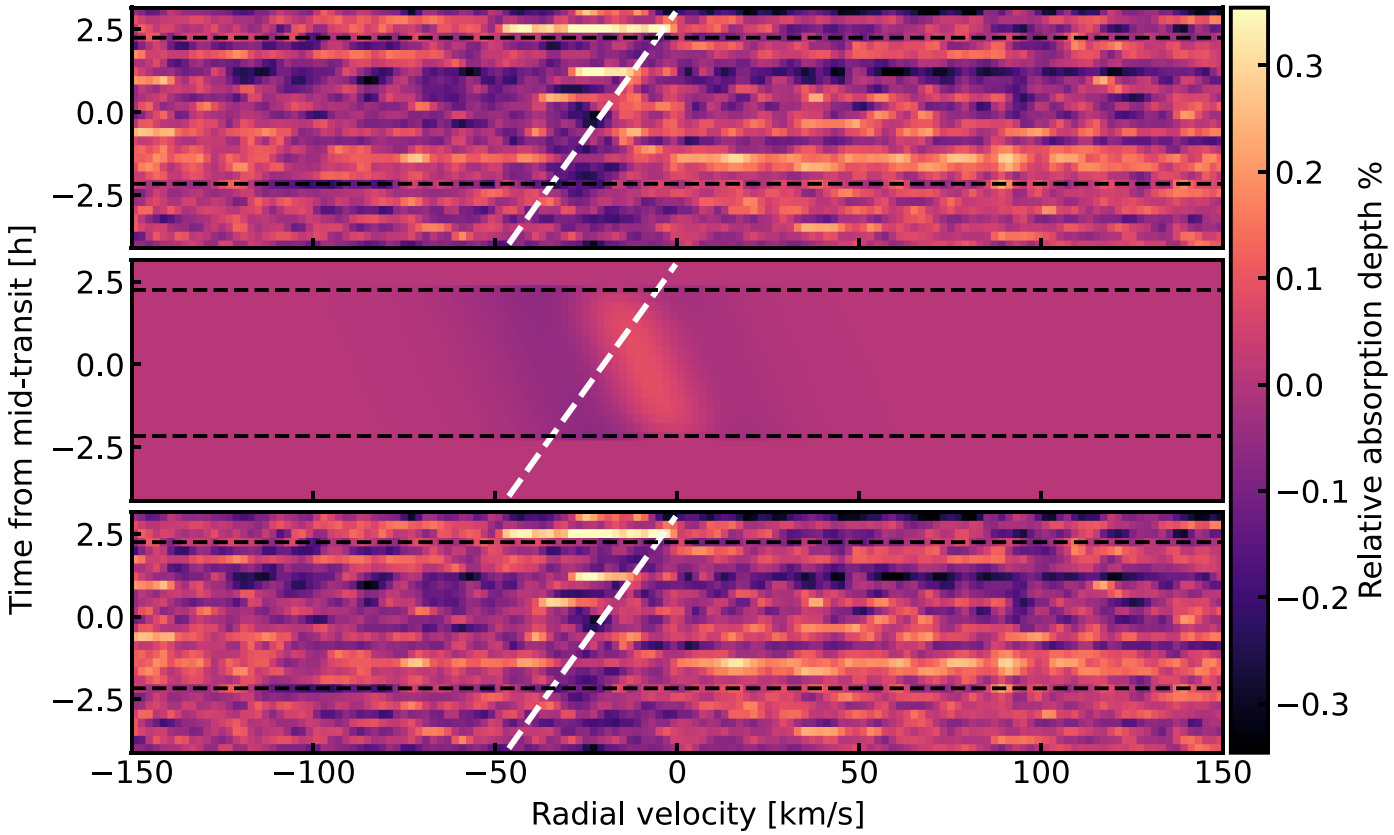

Fig. A.1. Correction of the residual of the planetary obscuration of the stellar disc (Doppler shadow). The planetary trace is shown in white. The dashed black lines indicate the start and the end of the transit. *Top panel:* Two-dimensional cross-correlation function. *Middle panel:* Model of the residual of the planetary obscuration of the stellar disc with two Gaussian components. *Bottom panel:* Two-dimensional cross-correlation function after correction.